Supporting information

Experimental Section

Atomic Force Microscopy: AFM experiments were performed on a NX10 system from Park-Systems, Korea. The AFM was positioned in a Glove-Box containing dry nitrogen atmosphere. KPFM measurements were performed with PPP-NCST-Au probes (Nanosensors, k=7.4 N/m) or NSC36/CrAu-B (Mikromasch k=2 N/m) following measurement procedures as described in literature[1]. Measurements were performed in dark, straylight of the AFM-beam (830 nm) had no impact on measurements.

Kelvin Probe: The contact potential difference measurements (CPD) were performed with a Kelvin probe consisting of a vibrating gold mesh driven by a piezo electric crystal (Kelvin probe S and CPD controller by Besocke Delta Phi). The samples were opened in air and quickly mounted in the setup, which was subsequently closed and evacuated until a pressure of roughly 0.5 mbar. The vacuum chamber was then refilled with N_2 until a pressure of approximately 670 mbar and, at this point, the measurement was started.

Electrochemical measurements: Cyclic voltammetry of the perovskite thin films with and without the tailored molecules (e.g. IPFC10 or csc5) coating on FTO glasses was performed in a three-electrode electrochemical cell using a potentiostat (Ivium Technologies B.V., Compact Stat). Experiments were carried out in an electrolyte containing 0.1 M Bu_4NPF_6 in dichloromethane. The thin film sample, a platinum wire, and an Ag/AgCl in saturated KCl were employed as a working, counter and reference electrode, respectively. The area of the working electrode that was exposed to the electrolyte was 0.785 cm^2. The measurements were conducted with a scan rate of 100 mV s^{-1}. A continuous nitrogen bubbling was applied on the electrolyte during the measurement to minimize the influence of oxygen on the determination of the redox potential. All measured potentials were correlated with the redox potential of Ag/AgCl, converting to energy level (CB and VB) vs. vacuum level: 1) $E_{VB} = E_{ox} + 4.65$; 2) $E_{CB} = 4.65 + E_{re,}$ where E_{ox} is the oxidized potential and E_{re} is the reduced potential.

	E_{ox}, V	E_{VB}, eV	E_{re}, V	E_{CB}, eV
FTO+perov	0,88	5,53	-0,91	3,74
FTO+perov+IC10	1,1	5,75	-0,25	4,37
FTO+perov+csc5	0,52	5,17	-0,14	4,51

Table S1: cyclic voltammetry results.

KP-APS: The Kelvin probe (KP) and the Ambient Pressure Photoemission Spectroscopy (APS) techniques are combined in a single KP-APS measurement tool provided by KP Technology Ltd. to determine the work function (WF) and the ionization energy of materials which defines the WF in case of metals and the valence band edge in case of semiconductors[2]. The KP system employs a 2.0 mm diameter tip with a gold alloy coating which is calibrated on a gold reference sample. The KP is placed in a Faraday cage which screens the external electrical fields. The contact potential difference (CPD) between tip and reference is measured with a resolution of up to 3 mV. The APS system uses the same Kelvin probe to detect the photoemission currents as a function of incident photon energy. The light source comprises a deuterium (D_2) lamp coupled with a grating monochromator. The range of the incident photon energy is 3.6-6.9 eV. The sample is illuminated via a DUV optical fiber. The photoemission threshold is determined with a resolution of 30 meV.

Devices preparation:

All chemicals without specifications were ordered from Sigma Aldrich and were used as received.

N-i-p devices were prepared on etched FTO substrates (TEC 15 from Ying Kou) with dimensions 2.5x2.5cm². Before use all the substrates were washed by sonication for 15 min. with Mucasol solution 2% in water (Schülke), DI water (only 5 min.), isopropanol and acetone respectively.

The washing procedure was followed by 15 min of O_3&UV treatment, then the samples were placed on a high temperature hot plate (Gestigkeit PZ28-3TD) for the compact TiO_2 sintering. TiO_2 compact layer was deposited by aerosol spray pyrolysis using oxygen as a carrier gas. The precursor solution for deposition on 27 substrates is: 0.48 mL of Acetylacetone (Santa Cruz Biotechnology) and 0.72 mL of titanium diisopropoxide bis(acetylacetonate) stock solution (75% in 2-propanol) diluted in 10.8 mL of ethanol (12 mL in total). The substrates were heated to 450 °C and kept at this temperature for 15 min before and 30 min after the spray of the precursor solution. The whole solution was sprayed using oxygen as carrying gas at a distance of 20 cm with inclination of 45°, with at least 20 s of delay between each spraying cycle.

The mesoporous TiO_2 was prepared by a spin coating step followed by sintering. The solution is made of TiO_2 paste (30 nrd, greatcellsolar) dissolved in ethanol (125 mg/ml). 80 µl of solution were spin coated at 4000 rpm for 10s, annealed for few minutes at 100 °C and then sintered in the same hotplate used for the compact TiO_2 at 450°C for 30 min (after ramping up to this values in about 40min).

Finally the substrates were treated with Li (LiTFSI in acetonitrile roughly 10mg/mL) right before the perovskite spin coating. 80 µl of Li solution were spin coated at 3000 rpm for 10s, annealed for few minutes at 100 °C and then sintered following the procedure in table 1.

All the steps mentioned so far were performed in air. All the following steps were performed in N_2-filled gloveboxes.

The perovskite solution (CsMAFA-perovskite) was prepared as follow. Stock solutions of PbI_2 (1.5 M, TCI) and $PbBr_2$ (1.5 M, TCI) in anhydrous DMF/DMSO = 4:1 (v:v) were previously prepared and heated again overnight at 60°C in a thermoshaker before use. MABr and FAI powders (dyenamo) were weighed out in two separate vials and then the proper volume of PbI_2 ($PbBr_2$) stock solutions was calculated and added to the vials containing the FAI (MABr) powder to get a stoichiometry of FAI:PbI_2 (MABr:$PbBr_2$) of 1:1.09. Before deposition, the solutions were mixed as follows: $FAPbI_3$:$MaPbBr_3$ = 85:15 (v:v). Further CsI (1.5 M) from a stock solution in DMSO was eventually added to the precursor solution to produce a final composition with the stoichiometry $Cs_{0.05}[MA_{0.15}FA_{0.85}PbI_{0.85}Br_{0.15}]_{0.95}$.

The samples were then taken to a N_2-filled glovebox for the perovskite spin coating. 80 µL of perovskite solution were then drop-casted the substrates and spin coated in a two-step program at 1000 rpm for 10 s and 6000 rpm for 20 s. 5 s prior to the end of the program, 100 µL of CBZ were poured on the spinning substrate. Afterwards, the samples were annealed at 100 °C for 1 h.

At this point the molecules were deposited on the substrates following the procedure shown in Fig. S1 and using solutions of csc5 (Alfa Aesar) dissolved in hexane with different concentrations.

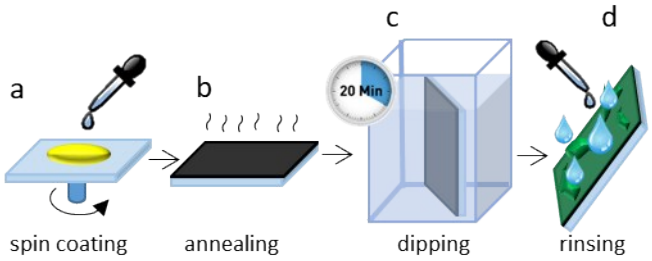

Figure S1. Description of the procedure for the molecules deposition: the perovskite is spin coated (a) and annealed (b), then the substrate is dipped for 20min in a solution of the desired molecule at a specific concentration (c) and finally rinsed with the solvent for removing agglomerates and residues (d).

After the molecules deposition, spiro-OMeTAD was spin coated on top of the samples. A 28.4mM solution of spiro-OMeTAD in chlorobenzene with additives (4-tert-Butypyridine, LiTFSI and Co(III)TFSI) was prepared using stock solutions.

The solution was then dynamically spin coated on the substrates: the solution was drop casted on the substrates right after the acceleration step (1.8 s at 200 rpm), a spinning step of 30s at 1800s rpm followed. Then, after storing inside a dry air box overnight, the samples were transferred into the thermal evaporator (Mbraun Pro Vap 3G) for the deposition of 80 nm gold. The active area resulting from the use of masks during the evaporation was 0.18 cm^2, area that was then, thanks to shadow masks, reduced to 0.1 cm^2 for the solar simulator testing.

The light JV of perovskite solar cells were recorded using a Wavelabs Sinus-70 LED class AAA solar simulator in air. The light intensity was calibrated with a Silicon reference cell from Fraunhofer ISE. JV scans were performed with a Keithley 2400 SMU, controlled by a measurement control program written in LabView. The voltage step was of 10 mV with an integration time of 50 ms per point and settling time of 50 ms after voltage application, corresponding to a scan rate of 100 mV/s.

Drift-Diffusion simulations

We adopted a finite element dirft-diffusion (DD) simulation model to understand the work-function shift at the perovskite/Spiro-OMeTAD interface. The model is implemented in TiberCAD multiscale simulation tool [3,4]. This is a well-established model, have already been used to simulate perovskite solar cells [5,6], organic solar cells [7,8], dye-sensitized solar cells [9–11] and organic and inorganic LED[12,13]. The model accounts for the optical generation of electron-hole pair in the perovskite film by absorbing sunlight, and the charge transport simultaneously. We mapped a planer solar cell architecture into a one-dimensional simulation model consisting electron selective layer (ESL), perovskite layer, hole selective layer (HSL), and to account for the interface traps, two buffers layers each if 2nm are considered each side of the perovskite layer, as shown in Fig. S2:

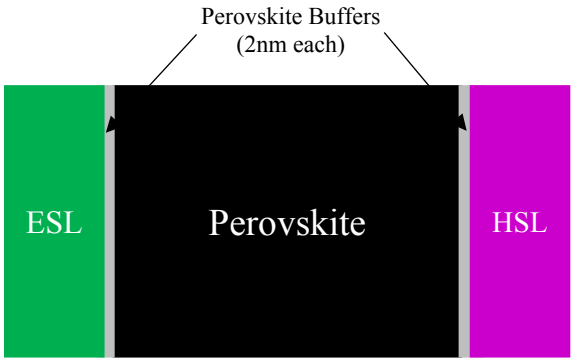

Figure S2: model for the solar cell in the drift-diffusion simulations.

Thickness of the perovskite, ETL and HTL layers were taken according to the experimental devices. The charge transport in the device is governed by diffusion and electrically induced drift, governed by the following set of equation:

$$\begin{cases} \nabla.(\varepsilon\nabla\phi) = -q(n - p + N_a^- - N_d^+ + n_t^- - n_t^+) \\ \nabla.\{\mu_n n(\nabla\Phi_n)\} = -R + G \\ \nabla.\{\mu_p p(\nabla\Phi_p)\} = R + G \end{cases}$$

Where, ε is the material the dielectric constant, ϕ the electrostatic potential, and q is the elementary charge. n is electron density, p hole density, N_a^- ionized acceptor density, N_d^+ ionized donor density, μ_n the electrons mobility and μ_p is the hole mobility. n_t^+ and n_t^- represent hole and electron trap concentrations respectively. Φ_n and Φ_p are the electrochemical potentials of electrons and the holes, respectively. The last two equations are the continuity equations for the electrons and holes. *R* and *G* describe net recombination and generation rates, respectively. Considering the Lambert-Beer model for absorption, the electron-hole pair generation at position x, is given as:

$$G(x) = \int_{\lambda_{min}}^{\lambda_{max}} \varphi(\lambda)\alpha(\lambda)\, e^{-\alpha(\lambda)x} d\lambda \quad ,$$

Where, $\varphi(\lambda)$ the solar light intensity and $\alpha(\lambda)$ is the perovskite absorption coefficient at wavelength λ. The AM 1.5 standard spectrum between 350nm and 1500 nm is used to calculate the optical generation. We considered the absorption coefficient to be weekly dependent on λ and hence use approximated $\alpha = 12\ \mu m^{-1}$ resulting in an exponential generation profile with a maximum electron-hole pair generation rate = $1.58x10^{22}\ cm^{-3}s^{-1}$. This maximum generation rate is obtained by matching the short-circuit current density of the experimental reference device.

To calculate net recombination rate *R*, two type of recombination processes are considered. First, radiative (direct) recombination defined as:

$$R_{dir} = k(np - n_i^2)$$

Where, k is the bimolecular recombination rate constant, and n_i is the equilibrium carrier concentration. The second, non-radiative recombination to include the effect of traps, given by the Shockley-Read-Hall recombination[14]:

$$R_{srh} = \frac{np - n_i^2}{\left(n + n_i e^{\frac{E_t}{k_B T}}\right)\tau_p + \left(p + p_i e^{\frac{E_t}{k_B T}}\right)\tau_n}$$

Where, $E_{trap} = -(E_c + E_v)/2$ is the trap energy level with respect to the midgap energy. τ_p and τ_n represent trapping times of the holes and the electrons, respectively. More number of traps leas more (and faster) trapping, and hence smaller values of trapping times. In the simulations, we considered acceptor and donor traps in the middle of the bandgap because recombination is most effective when the traps are located in the midgap[15]. Perovskite cells have more number traps at the interface compared to the bulk, hence smaller value of τ_n and τ_p are chosen at the interface. Mobility value in different layers are extracted from the fitting parameters which are very close to the values available in literature. More details of the parameters used in the simulation are provided in the table S2.

Table S2: List of the parameters used in the drift-diffusion simulation model

Parameter	Value	Unit	References
Electron and hole mobility in Perovskite	5	cm^2/Vs	[16]
Perovskite valence band	-5.53	eV	
Perovskite conduction band	-3.89	eV	
Perovskite relative permittivity	23		fit
TiO_2 bandgap	3.25	eV	[17]
TiO_2 HOMO	-7.2	eV	[18]
Electron mobility in TiO_2	5×10^{-3}	cm^2/Vs	fit
TiO_2 relative permittivity	85		[18]
Spiro-OmeTAD bandgap	3.17	eV	[19]
Spiro-OmeTAD HOMO	-5.3	eV	fit
Spiro-OmeTAD relative permittivity	3.53	eV	[20]
Hole mobility in Spiro-OMeTAD	3×10^{-3}	cm^2/Vs	fit
Acceptor doping in Spiro-OMeTAD	4.8×10^{17}	cm^3	fit
$\tau_{n,p}$ bulk film	1×10^{-7}	Sec.	[21]
$\tau_{n,p}$ interface buffers	$1\times10^{-10} - 3.2\times10^{-10}$	Sec.	fit
Anode fermi level	-4.1	eV	[22]
Cathode fermi level	-5.1	eV	[23]
Bimolecular recombination rate	5×10^{-11}	cm^3s^{-1}	[21]
Maximum optical generation rate	1.58×10^{22}	cm^3s^{-1}	fit

The model simulated the steady-state performance of the cell. It is known that the perovskite films consist of ionic defects and the ions are most effective when they accumulate near the interfaces[24]. To account for the impact of ionic defects, 1×10^{17} cm^{-3} ions are considered in the buffer regions. To obtain a good fitting and the experimental trend for higher concentrations of the Lewis base, and need to be changed to lower values such as 1.0×10^{-10} Sec. This infers that the interface deteriorates (the number of traps might increase and or the Lewis base material may deposit a low conductive layer at the perovskite/HSL interface) upon the use of higher concentration. This results in a reduction in the FF in spite of increasing the open-circuit voltage, as obtained from the experiment.

DFT simulations

Method:

We investigate the interaction of amyl sulfide (csc5) and Perfluorodecyl iodide (IPFC10) molecules on the surface of $MAPbI_3$ perovskite. We consider only the (001) surface and we investigate three different surface terminations, namely a PbI_2-terminated, a 50%-MAI terminated (thus 50% PbI_2-terminated) and a fully MAI-terminated surface. These represent the limiting cases where the surface is fully unpassivated, half passivated and fully passivated by MAI units[25].

DFT calculations were performed within the supercell approach. Slabs models were built starting from the tetragonal phase of $MAPbI_3$, by fixing cell parameters to the experimental values[26]. 10 Å of vacuum were added along the non-periodic direction perpendicular to the slabs in all cases. To simulate the aforementioned different MAI coverages of the (001) surface, the $MAPbI_3$ 2x2 in-plane supercells were constructed by progressively removing MAI units. To achieve a flat electrostatic potential in the vacuum region a symmetric disposition of the organic cations and of the adsorbed molecules on the external layers of the slabs was adopted in all cases, leading to supercells with zero average dipole moments.

As previously found, surface termination (or coverage) has a strong impact on the perovskite work function (WF)[25]. PbI_2-terminated show the highest WF (6.4 eV, Table S3), MAI-terminated show the lowest WF (4.7 eV) and intermediate MAI coverages show intermediate WF values (5.3 eV for 50:50 coverage, Table S3). Based on our analysis a WF of 4.9 eV (as experimentally found) would correspond to about 20-30% of the surface being unpassivated.

The work function was calculated employing the PBE[27] and hybrid HSE06 functionals[28], in the last case by including spin-orbit coupling (SOC) and an increased fraction of exact exchange α=0.43. Semi-local functionals like PBE, in fact, do not provide an accurate description of the electronic properties of perovskites due to self-interaction error, while the use of hybrid HSE06 functional with an increased fraction of exact exchange α=0.43,4 SOC included, provides an accurate estimate of the electronic properties of $MAPbI_3$ in agreement with state of the art GW calculations and experiments[29,30]. By using the HSE06-SOC functional a down-shift of the VBM energy of 0.5 eV is obtained with respect to the PBE calculation for bulk $MAPbI_3$, in agreement with previous studies[31]. In order to obtain HSE06-SOC values in Table S3, the down-shift of the VBM found at the hybrid SOC level for bulk $MAPbI_3$ has been rigidly applied to the work function values computed at the PBE level after aligning the electrostatic potential of the bulk to the potential in the internal region of the slab.

For PBE calculations we employed ultrasoft pseudopotentials (shells explicitly included in calculations: I 5s, 5p; N, C 2s, 2p; O 2s 2p; H 1s; Pb 6s, 6p, 5d) and a cutoff on the wavefunctions of 40 Ryd (320 Ryd on the charge density). We sampled the Brillouin zone at the k-point Γ. Hybrid HSE06-SOC calculation on the unit cell of bulk $MAPbI_3$ has been carried out by using norm-conserving pseudopotentials (shells explicitly included in calculations: I 5s, 5p; N, C 2s, 2p; H 1s; Pb 5s, 5p, 5d, 6s, 6p) with an energy cutoff on the wavefunctions of 40 Ryd and a 2x2x2 k-points grid in the BZ. All calculations were performed by using the Quantum Espresso package.

The work function of the systems have been estimated by using the expression

$$WF = V(vacuum) - E(VBM) \qquad (2)$$

where V(vacuum) is the electrostatic potential in the vacuum, i.e. the sum of the pseudo and Hartree potentials (VPS + VH) in the vacuum region between periodic slabs, and E(VBM) is the energy of the top of the valence band of bulk $MAPbI_3$. The VBM of bulk $MAPbI_3$ used in Equation 2 were obtained by following an alignment procedure of the electrostatic potential in the slab and in the bulk $MAPbI_3$.

Work function (WF) analysis:

We investigate how the csc5 or IPFC10 adsorption may influence the WF values for the three considered systems. Starting from case (A) in Table S3, we notice that while csc5 has a significant adsorption energy on undercoordinated surface Pb atoms, IPFC10 has a smaller thermodynamic energy gain to be adsorbed on the PbI_2-teminated surface. Adsorption geometries are reported in Fig. S4a-b, showing the clear formation of a Pb-S bond in the case of csc5, while IPFC10 adsorption results in the establishment of a Pb-I bond and an interaction with a lateral surface iodine, suggesting the concomitant formation of a metal-halide and halogen bonds. The reason why adsorption energies favor csc5 is ascribed to the stronger Pb-S bond formed.

Table S3. Adsorption energies, work functions and work function shifts with the respect of the reference pristine PbI_2-terminated, Half terminated (50% MAI – 50% PbI_2), MAI terminated and 87.5% MAI terminated surfaces respectively, computed at the PBE and HSE06(0.43)-SOC level of theory. In the case of the Half terminated (50% MAI – 50% PbI_2) slab the molecular coverage spans up to an extended range to investigate higher surface concentrations of csc5 and IPFC10.

System	**Molecular Coverage**	**Adsorption energy (eV)**	**Adsorption energy / molecule (eV)**	**WF PBE (eV)**	**WF Shift PBE (eV)**	**WF HSE06(0.43)-SOC (eV)**	**WF Shift HSE06(0.43)-SOC (eV)**
	PbI_2-terminated (A)						
Pristine	**0.0**	**-**	**-**	**5.975**	**-**	**6.416**	**-**
csc5 / surface	0.125	-0.75	-0.75	5.569	-0.406	5.819	-0.597
2 csc5 / surface	0.250	-1.31	0.66	5.260	-0.714	5.521	-0.894
IPFC10 / surface	0.125	-0.32	-0.32	5.981	0.006	6.327	-0.089
2 IPFC10 / surface	0.250	-0.59	-0.30	5.985	0.011	6.301	-0.115
	Half-terminated (50% PbI_2 / 50% MAI) (B)						
Pristine	**0.0**	**-**	**-**	**5.226**	**-**	**5.309**	0.00
csc5 / surface	0.125	-0.56	-0.56	4.946	-0.279	5.010	-0.299
2 csc5 / surface	0.250	-0.67	-0.33	4.785	-0.441	4.818	-0.491
3 csc5 / surface	0.375	-0.97	-0.32	4.510	-0.715	4.571	-0.738
5 csc5 / surface	0.625	-1.07	-0.21	4.274	-0.952	4.252	-1.057
6 csc5 / surface	0.750	-1.18	-0.19	4.207	-1.018	4.258	-1.050
IPFC10 / surface	0.125	-0.25	0.00	5.516	0.291	5.614	0.305

2 IPFC10 / surface	0.250	-0.51	-0.24	5.772	0.547	5.845	0.537
4 IPFC10 / surface	0.500	-1.05	-0.25	6.139	0.914	5.611	0.905
6 IPFC10 / surface	0.750	-1.48	-0.26	5.917	0.692	6.213	0.701
8 IPFC10 / surface	1.000	-1.82	-0.25	5.841	0.616	5.995	0.687
		MAI-terminated (C)					
Pristine	**0.0**	**-**	**-**	**4.617**	**-**	**4.668**	**-**
csc5 / surface	0.125	-0.02	-0.02	4.496	-0.121	4.553	-0.114
IPFC10 / surface	0.125	-0.27	-0.27	4.878	0.260	4.919	0.252
2 IPFC10 / surface	0.250	-0.52	-0.26	5.108	0.490	5.100	0.431
		87.5% MAI terminated (D)					
Pristine	-	-	-	**4.740**	-	**4.739**	**-**
csc5 / surface	0.125	-0.41	-0.41	4.544	-0.196	4.627	-0.112
IPFC10 / surface	0.125	-0.22	-0.22	4.794	0.054	4.841	0.101

Wf variations are also significant for csc5 adsorption, with a WF reduction of ca. 0.6 eV, while they are marginally influenced by IPFC10. This is likely the result of the two different bonds (Pb-I and I-I) compensating each other (see Charge Transfer Analysis).

A similar trend is found also for case (B), i.e. for the 50:50 surface. Despite the different adsorption sites, Fig. S4c-d, csc5 interaction with the surface is still favored. In the IPFC10 case adsorption is found to take place exclusively through halogen bond, Figure S4d. A drastically opposite WF trend is found for the two molecules with a WF decrease (increase) of ca. 0.3 eV for csc5 (IPFC10) adsorption.

We finally considered the fully passivated MAI-terminated surface (C) and the same surface where a MAI vacancy was created (D). The results were consistent with what found previously for IPFC10, if it forms halogen bonds (Figure S4f) we find a significant WF increase(C), which again scales almost linearly with the IPFC10 coverage, whereas if it falls in a situation analogue to the one of Fig S4b, low WF difference is recorded (D). In the case of csc5 we found a work function decrease in (D) and no significant contribution in (C) (Figure S4e).

To sum up, under all considered adsorption situations csc5 provides a WF reduction while IPFC10 leads to a WF increase or to a negligible decrease.

The simulations clearly indicate that while csc5 may preferentially interact with undercoordinated Pb atoms, leading to a WF decrease, IPFC10 can interact both with Pb or I surface atoms, forming different bonds whose contribution to the WF partially cancels out, however a net WF increase is observed in the majority of the cases.

The study of WF shift has been extended simulating coverage up to 1.0 on the 50% terminated surface, see Fig. S3c. At high molecular coverages a saturation of the WF shift is observed. This is consistent with the trend of total adsorption energies (Fig. S3d), indicating the complete passivation of the external layer. The slight decrease of WF for IPFC10 in Fig. S3c is ascribed to the formation of IPFC10-Pb bonds on the saturated surface which partially decrease the WF.

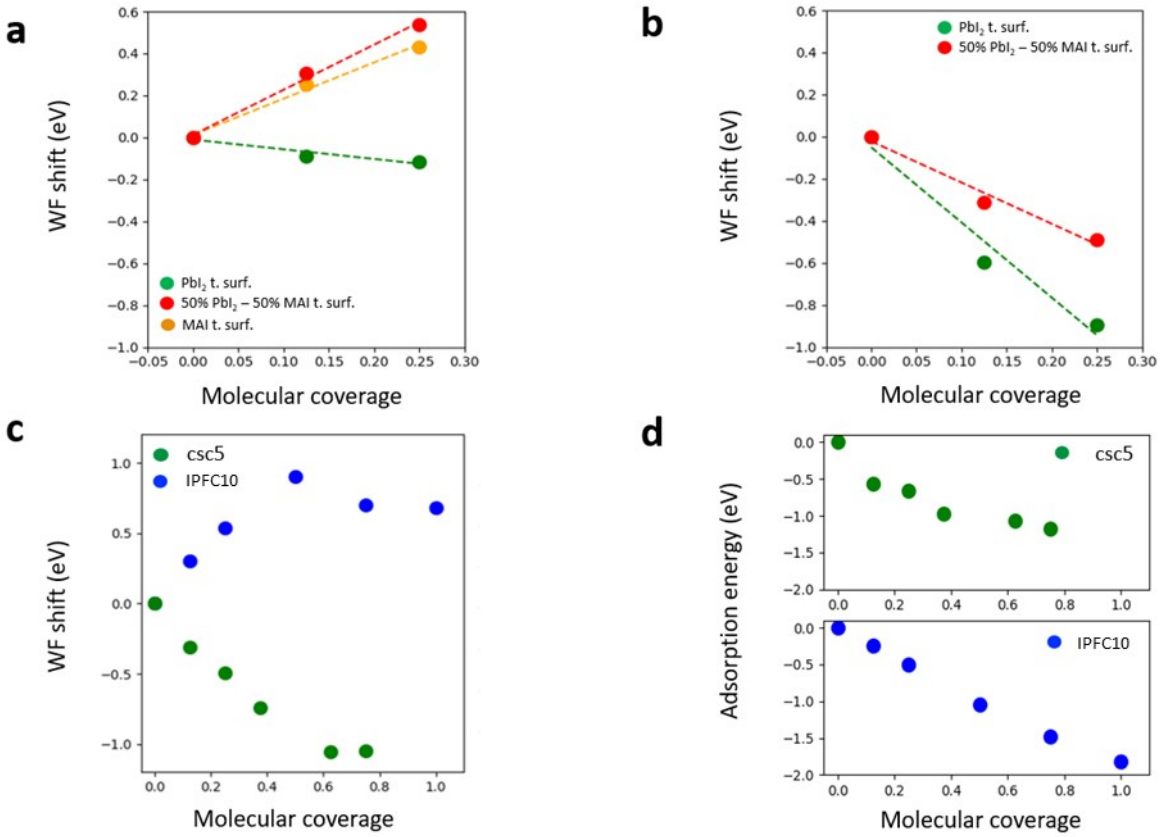

Figure S3. Comparison of work function shift versus molecular coverage upon IPFC10 (a) and csc5 (b) adsorption on different terminated (001) surfaces. Orange points represents molecules adsorbed on the (001) MAI terminated surface, red ones molecules adsorbed on the (001) 50% MAI-PbI_2 surface and green ones molecules adsorbed on the (001) PbI_2 surface. The extended trend of WF shift vs molecular coverage upon adsorption onto the (001) 50% MAI-PbI_2 surface is reported in (c) for IPFC10 and for csc5, the respective adsorption energies diagrams are reported in the panel (d).

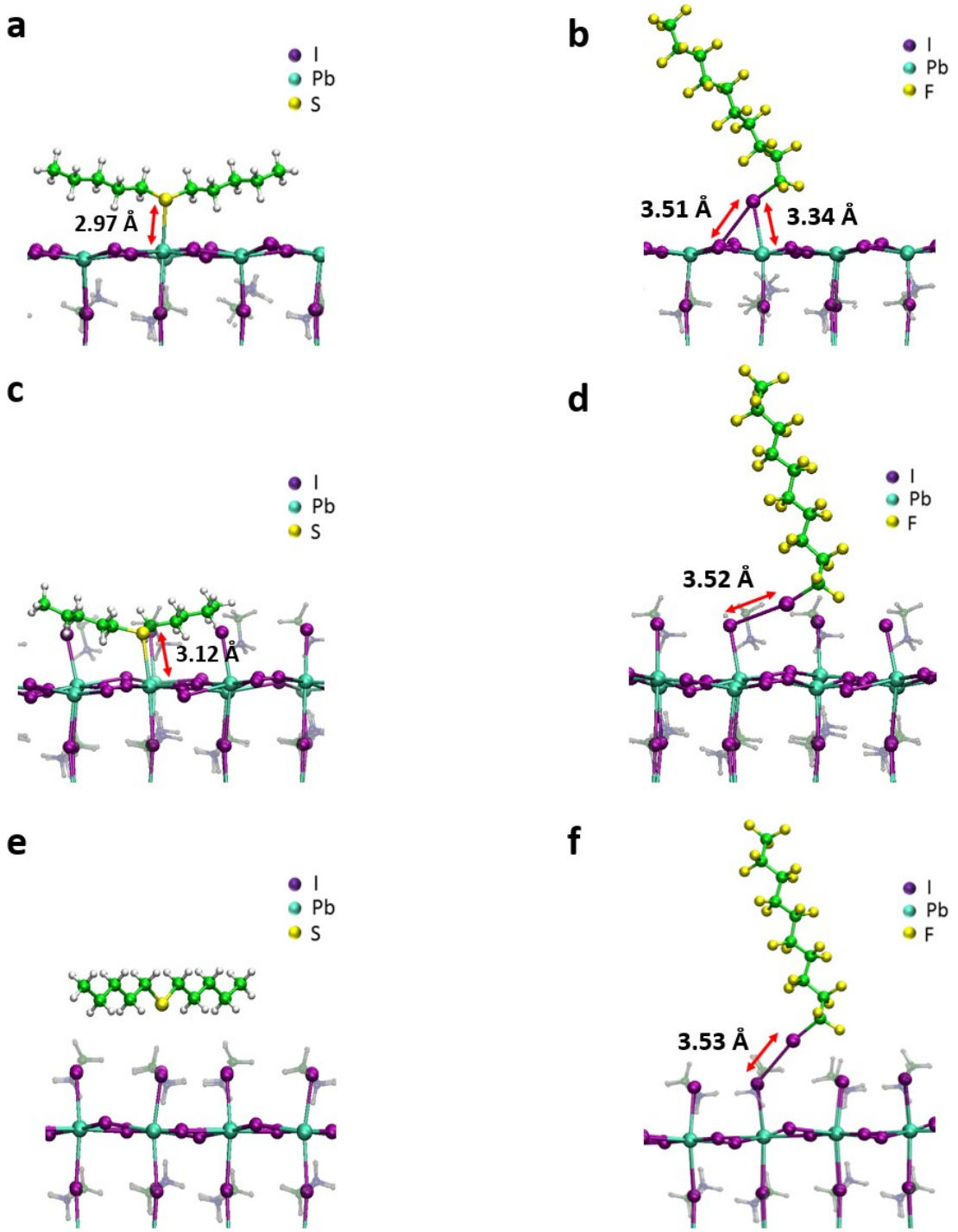

Figure S4. Optimized Structures of csc5 and IPFC10 anchored to a perovskite PbI_2-terminated surface (a) and (b), to a perovskite half 50 % PbI_2 - 50 % MAI terminated surface (c) and (d) and to a perovskite MAI-terminated surface (e) and (f). Bond lengths in Å.

Charge transfer analysis

To understand the origin of the WF shift we studied the charge transfer between the adsorbed molecule and the surface in the different cases.

The variation of the charge density upon the molecule adsorption has been evaluated by calculating the charge density difference between the molecule+slab system and the single components at fixed geometries

$\Delta\rho = \rho_{total} - \rho_{surface} - \rho_{molecule}$

A positive $\Delta\rho$ is consistent with an accumulation of electronic charge upon adsorption.

The planar averaged $\Delta\rho$ profile along the perpendicular direction to the slab are reported in Fig. S5-6 for the different cases. In the case of csc5 (Fig. S5) an accumulation of electronic charge is reported around the coordinated Pb at the surface, while a depletion is noted in the molecular region. This is consistent with the formation of a dipole at the interface pointing outwards and reducing the WF. The opposite is observed for the IPFC10 molecule where a depletion and an accumulation of charge is reported on Pb and the molecule, respectively.

To quantify the transferred charge ($CT_{molecule}$) the $\Delta\rho$ planar average has been integrated along the z-axis (see lower panels of Fig. S5 and S6) in the interval that spans from the position of the last PbI_2 perovskite layer to the end of the cell, covering the entire molecule region

$$CT_{molecule} = \int_{cell} dx \int_{cell} dy \int_{molecule} \Delta\rho(x,y,z)\, dz \qquad (1)$$

Computed $CT_{molecule}$ values are reported in Table S4. Positive values highlight electronic density accumulation at the molecule region, while negative ones electron density depletion. Furthermore, the dipole moments of the adsorbed molecules were evaluated by performing a single point on the molecules attached to the various perovskite surfaces employing the PBE functional along with the TZ2P basis set implemented in the ADF program.

We find a nice correlation of the computed work function shifts with the charge transfer (CT) of the anchored molecule (Fig. S7). In the case of csc5 (Fig. S7a) we observe smaller work function shifts by increasing the concentration of MAI on the surface that well correlates with the decreased charge transfer at the interface. This is likely due to the greater steric repulsion between the csc5 alkyl chains and the progressively filled MAI layer, hindering the bond and charge transfer.

Turning to IPFC10, we observe similar charge transfers and WF shifts for the half PbI_2-MAI and MAI terminated surfaces. A different behavior is reported for the PbI_2 terminated surface where the bond between the molecule and the surface is of different nature, involving bonds between the molecule halogen and both Pb and I of the surface. We register a nice correlation of WF shifts with the computed CT (Fig. S7b).

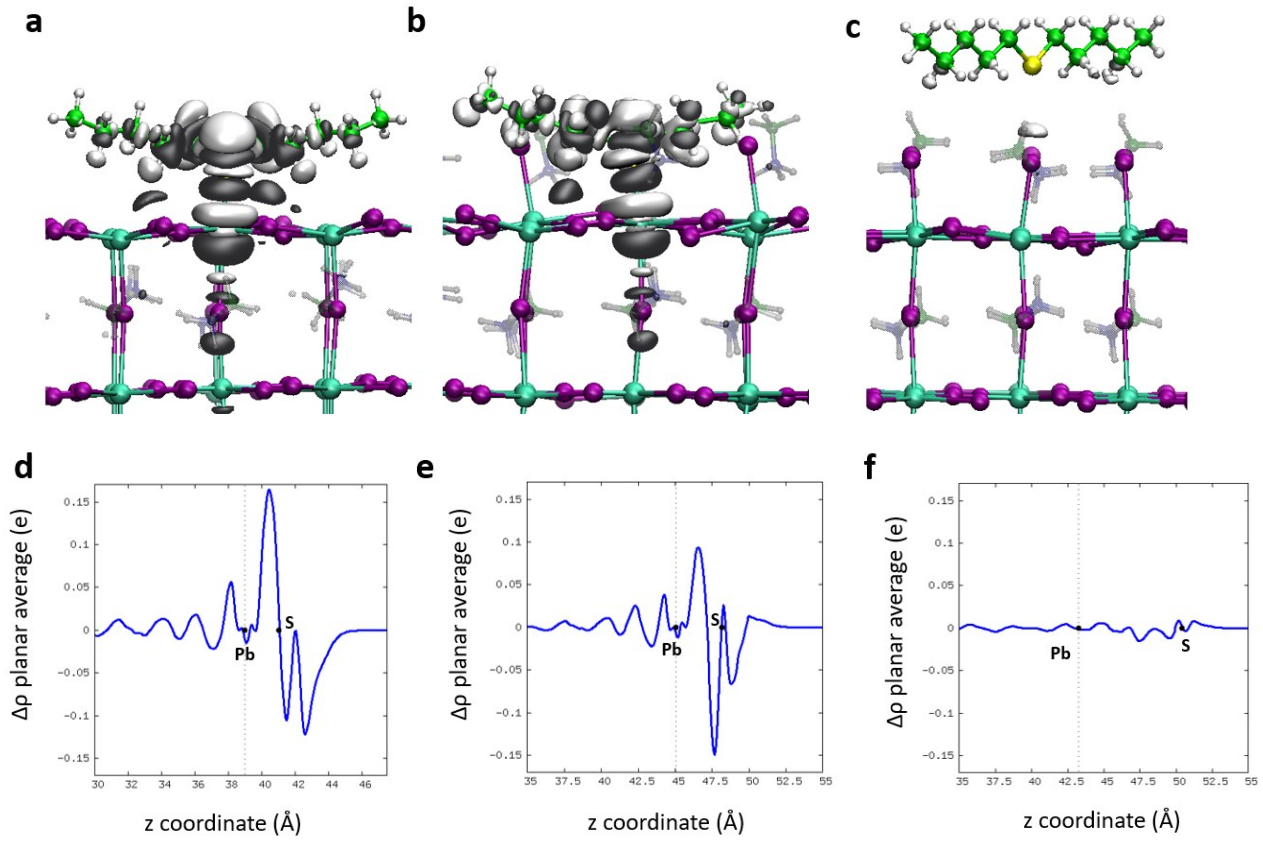

Figure S5. Iso-density plots *(a),(b),(c)* and planar average along the z-axis *(d),(e),(f)* of $\Delta\rho = \rho_{total} - \rho_{surface} - \rho_{molecule}$ for the csc5 molecule attached to *(a)(d)* PbI_2 terminated, *(b)(e)* half PbI_2 – MAI terminated and *(c)(f)* MAI terminated surfaces. The contour value for the iso-density plots is 0.0006. Positive charge density regions (charge accumulation) are highlighted in black, negative ones (charge depletion) in white. In the diagrams of $\Delta\rho$ planar average along the z-axis, the positions of the central Pb atom at the last PbI_2 layer of perovskite and of the molecule S atom are reported.

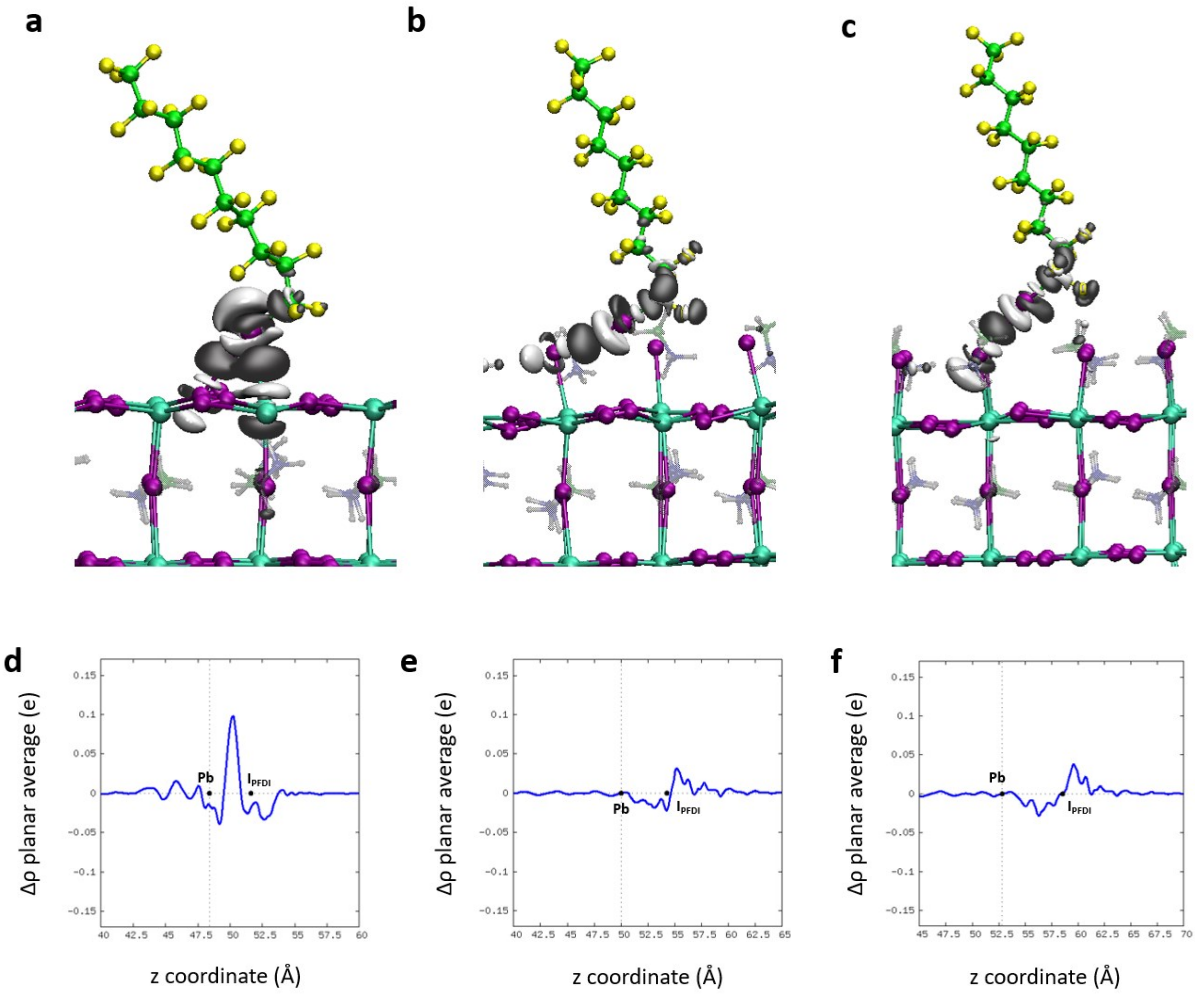

Figure S6. Iso-density plots *(a),(b),(c)* and planar average along the z-axis *(d),(e),(f)* of $\Delta\rho = \rho_{total} - \rho_{surface} - \rho_{molecule}$ for the IPFC10 molecule attached to *(a)(d)* PbI_2 terminated, *(b)(e)* half PbI_2 – MAI terminated and *(c)(f)* MAI terminated surfaces. The contour value for the iso-density plot is 0.0006. Positive charge density regions (charge accumulation) are highlighted in black, negative ones (charge depletion) in white. In the diagrams of $\Delta\rho$ planar average along the z-axis, the positions of the Pb atom at the last PbI_2 layer of perovskite and of the molecule I atom are reported.

Table S4. Dipole moments of the adsorbed molecules in the various cases calculated with B3LYP and PBE functionals and charge transfer to the molecule evaluated employing formula *(1).*

Adsorbed molecules	**Coverage**	**PBE (μ_x, μ_y, μ_z), μ adsorbed molecule (Debye)**	**PBE $CT_{molecule}$ (e)**
		PbI_2-terminated (A)	
csc5	1/8	(-1.119, 0.058, 0.937), 1.461	-0.05812
IPFC10	1/8	(-0.448, 0.234, -0.470), 0.693	-0.00939
		Half-terminated (50% PbI_2 / 50% MAI) (B)	
csc5	1/8	(-0.830, 1.044, 0.678), 1.496	-0.03949
IPFC10	1/8	(-0.810, 0.193, -0.775), 1.137	0.00807
		MAI-terminated (C)	
csc5	1/8	(-0.011, -0.022, 1.335), 1.335	-0.01062
IPFC10	1/8	(-0.724, -0.121, -0.730), 1.035	0.00978

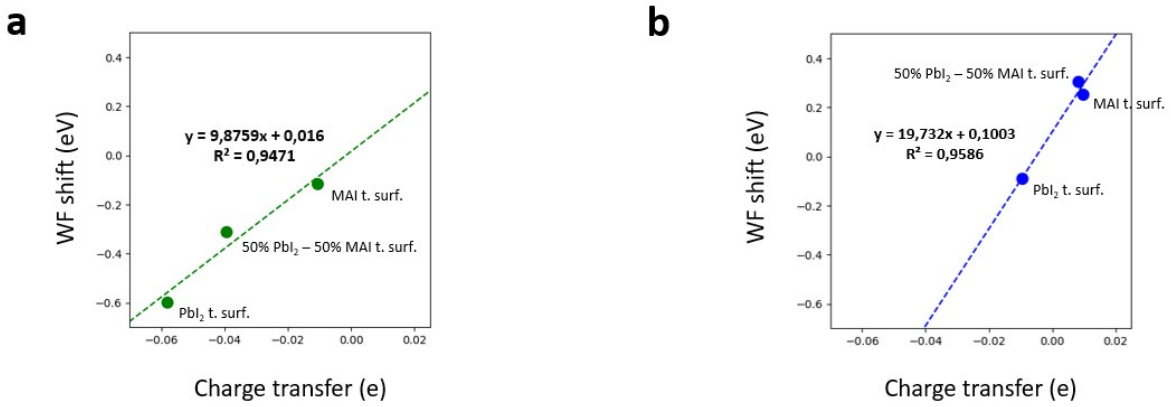

Figure S7. Diagrams of WF Shift vs Charge Transfer for the csc5 (a) and IPFC10 (b) molecules.

	x component	y component	z component	Total dipole
F-IC12	0,10324	0,16869	-0,22772	0,76665
topo	0,06094	0,11825	-1,39308	3,55704

Table S5. Dipole moments of the other molecules divided by component calculated with DFT simulations

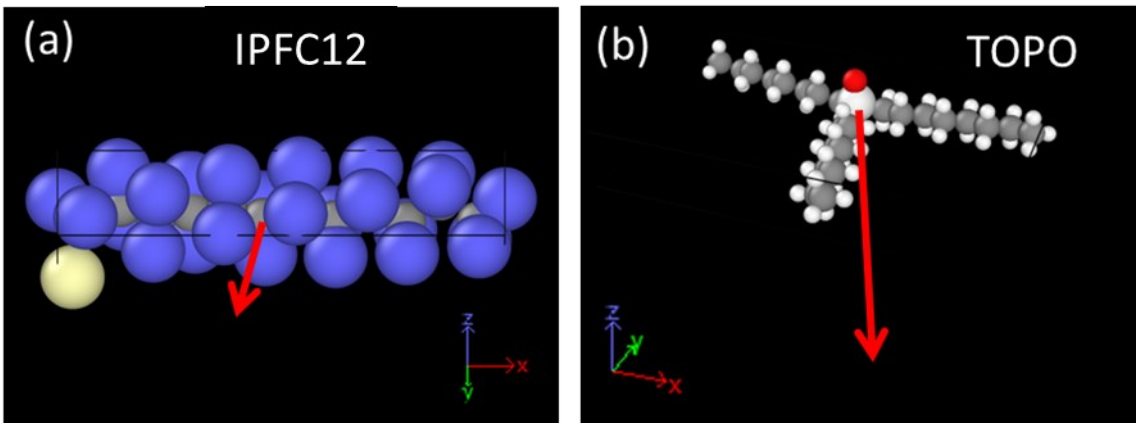

Figure S8. Representation of the other molecules and relative dipole through the software OVITO. The dipole is defined as pointing to the positive side. Blue is F, yellow is I, dark grey is C, light grey is H, Red is oxygen.

	CPD (± 2 mV)		SPV (± 3 meV)	Work function (± 0.04 eV)		Ionization energy (IE) (± 0.03 eV)	E_F - E_{VBM} (± 0.05 eV)	
	dark	illum.		dark	illum.		dark	illum.
perovskite	-5	135	140	4.96	5.10	5.54	0.58	0.44
CSC5	-156	-30	126	4.80	4.92	5.43	0.64	0.51
IPFC10	124	203	79	5.08	5.16	5.69	0.61	0.53

Table S6. Results of the KP-APS measurement. APS (light blue) and Kelvin Probe (light yellow) data were collected during the same measurement in order to have an idea of the whole band diagram.

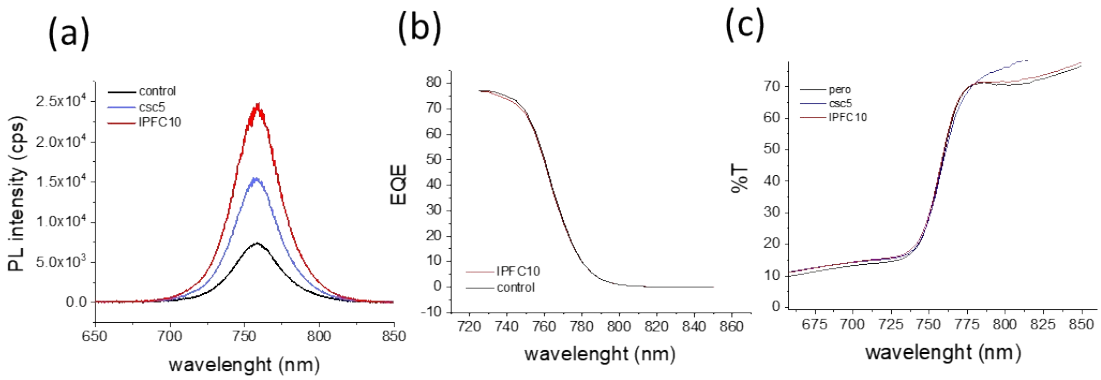

Figure S9. PL (a), EQE (b) and UV-Vis (c) of bare and functionalized perovskite showing that the bandgap is not changing. PL and EQE performed in N_2 atmosphere, UV-Vis performed in air.

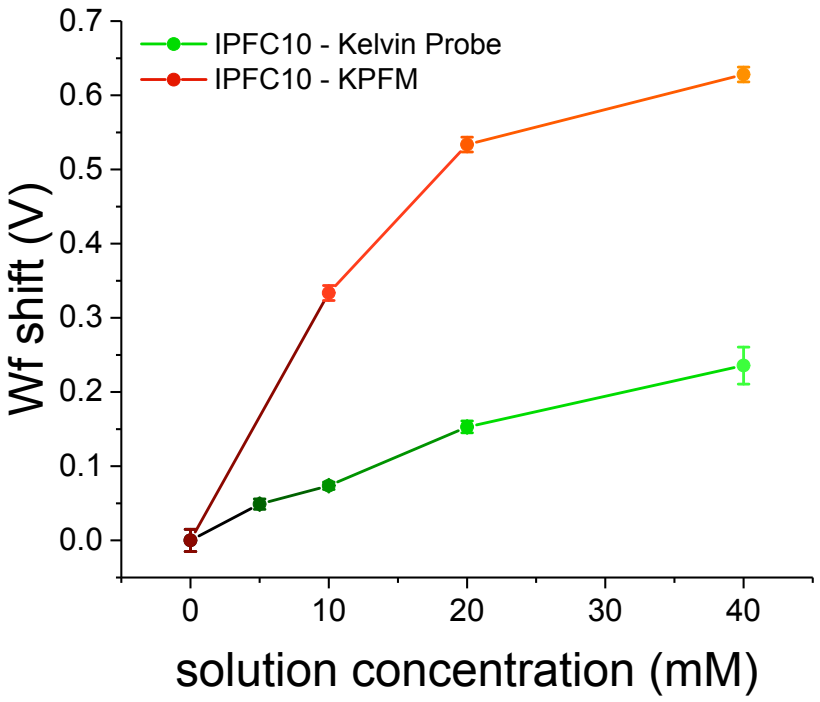

FigureS10. Comparison between Kelvin Probe and KPFM measurements proving that both measurements show the same trend. The magnitude of the shift is different because of the different measurement conditions, mainly the fact that Kelvin Probe was measured in air while KPFM in N_2.

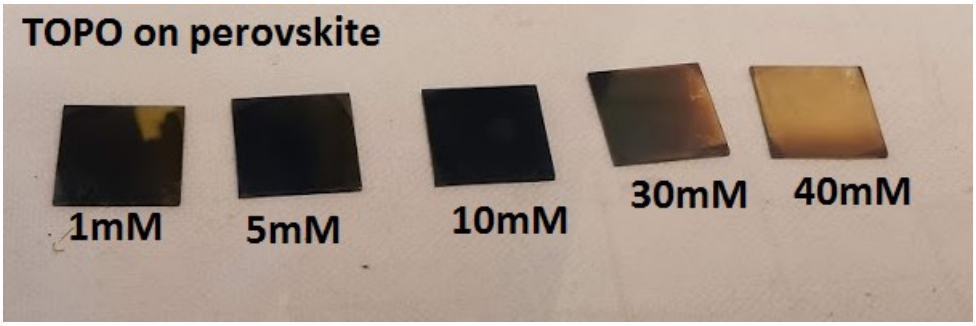

Figure S11. Effect of the deposition of TOPO on top of perovskite by dipping the substrates for 20min in TOPO solutions of different concentrations.

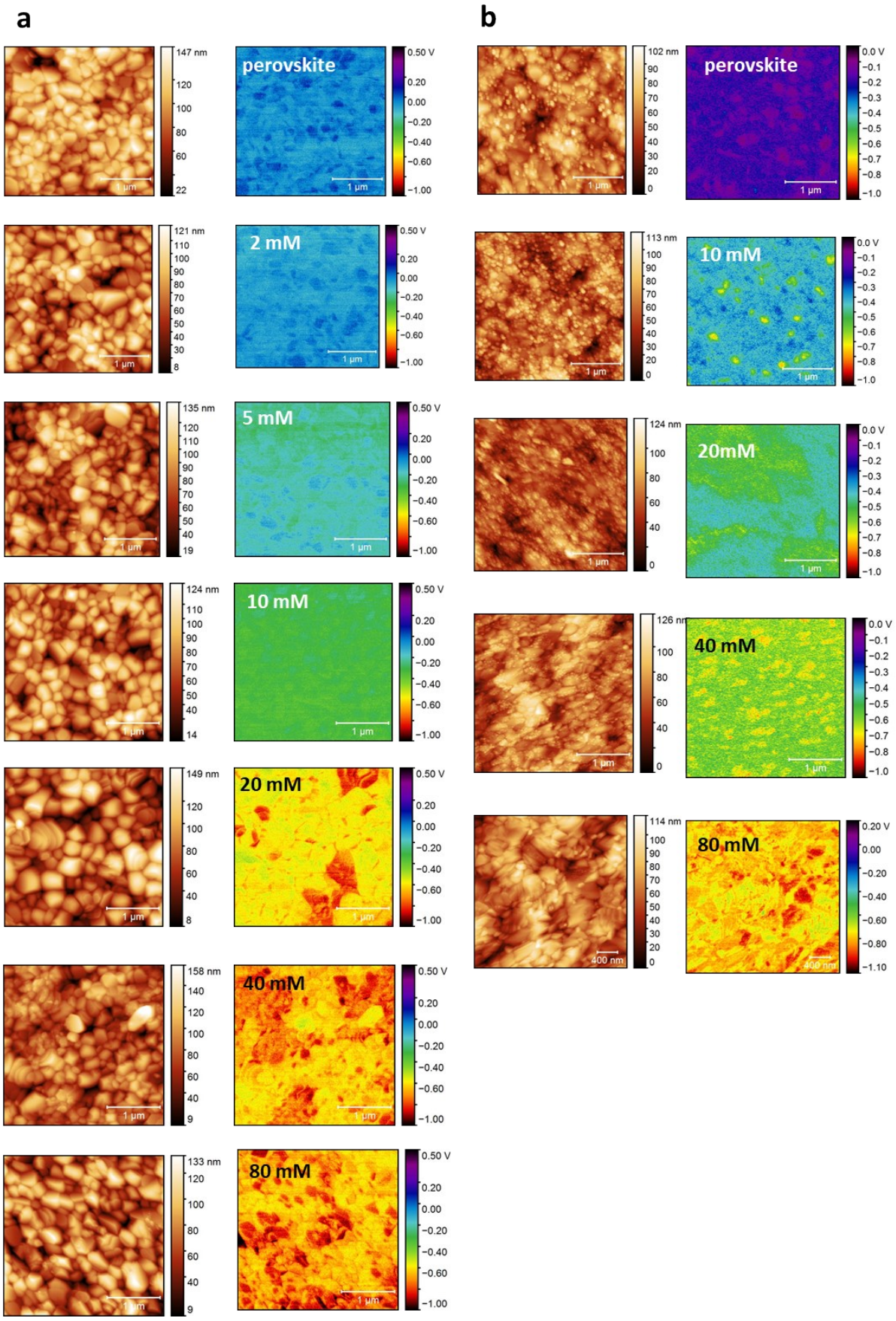

Figure S12. CPD and AFM maps for IPFC10 (a) and IPFC12 (b) at different concentrations.

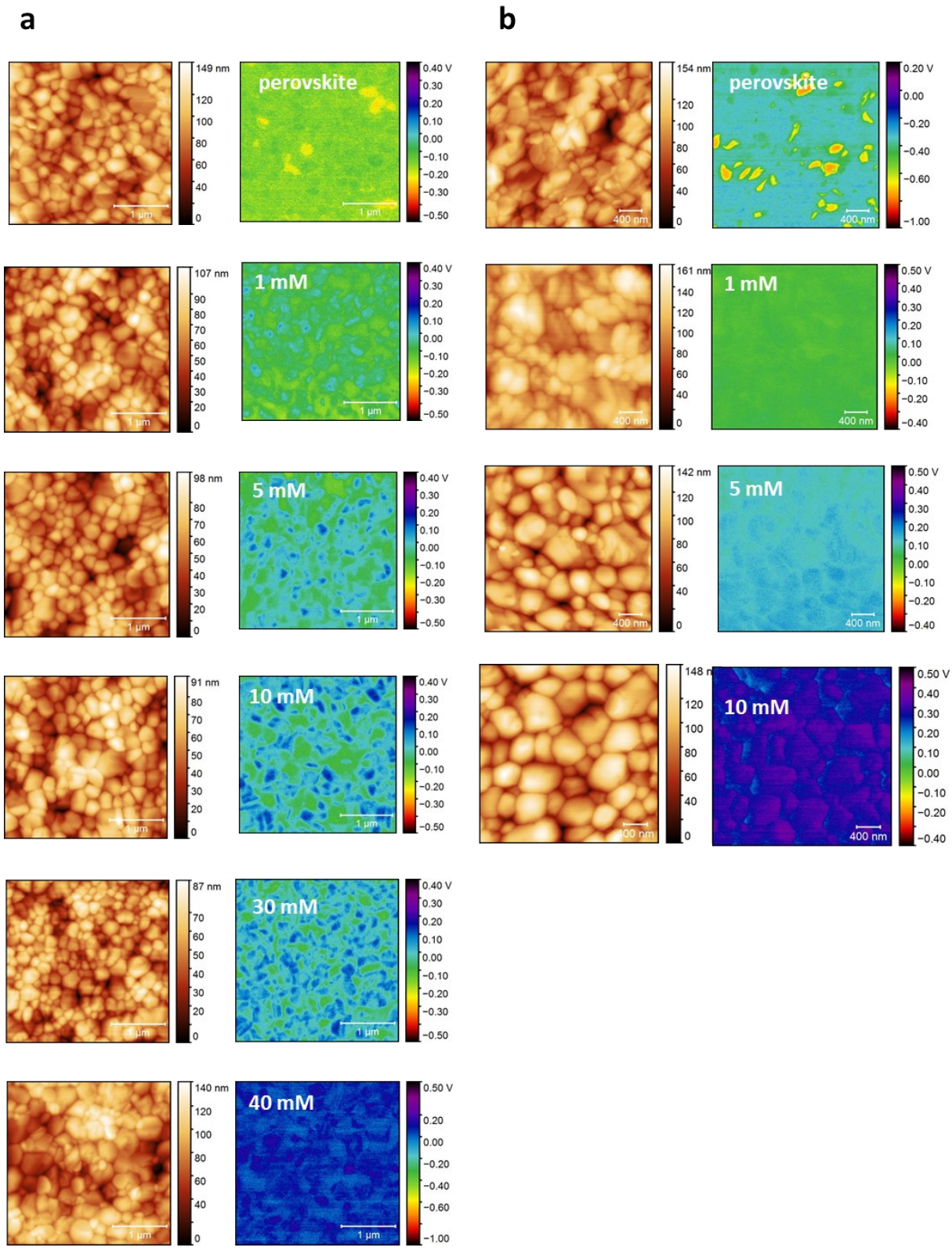

Figure S13. CPD and AFM maps for csc5 (a) and TOPO (b) at different concentrations.

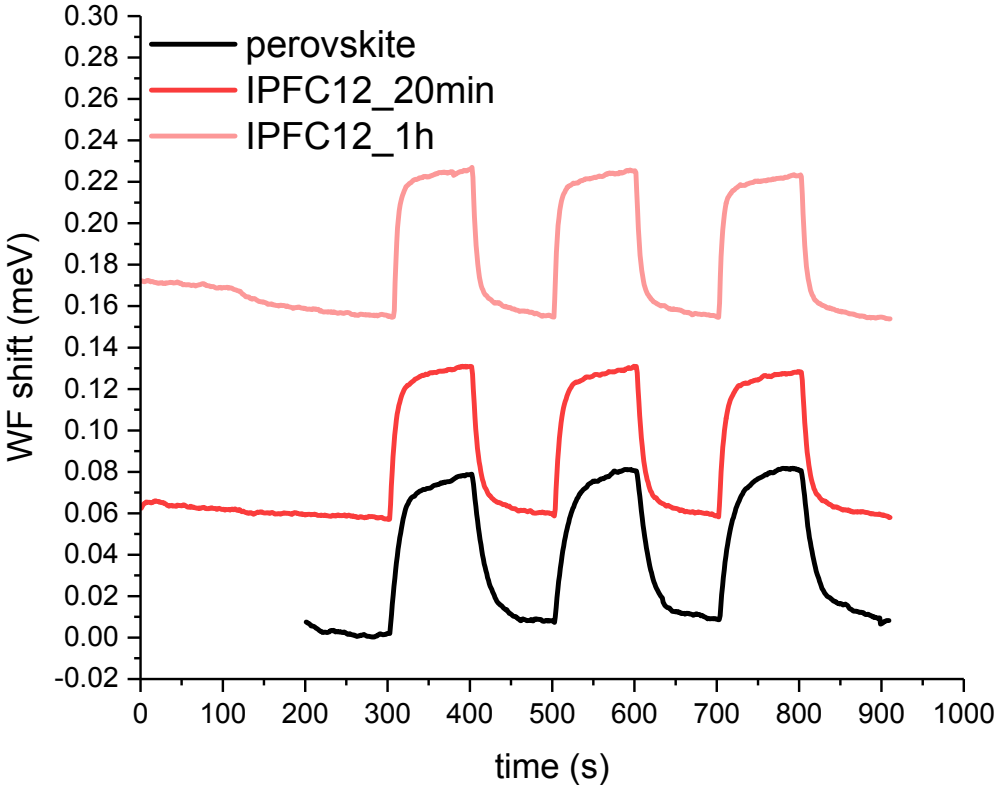

Figure S14. Kelvin probe WF shift measurement in dark and lught of perovskite functionalized with IPFC12 for different dipping times.

1 T. Cramer, L. Travaglini, S. Lai, L. Patruno, S. De Miranda, A. Bonfiglio, P. Cosseddu and B. Fraboni, *Sci. Rep.*, 2016, **6**, 1–9.

2 I. D. Baikie, A. C. Grain, J. Sutherland and J. Law, *Appl. Surf. Sci.*, 2014, **323**, 45–53.

3 M. Auf Der Maur, G. Penazzi, G. Romano, F. Sacconi, A. Pecchia and A. Di Carlo, *IEEE Trans. Electron Devices*, , DOI:10.1109/TED.2011.2114666.

4 A. Gagliardi, M. Auf Der Maur, D. Gentilini, F. Di Fonzo, A. Abrusci, H. J. Snaith, G. Divitini, C. Ducati and A. Di Carlo, *Nanoscale*, 2015.

5 A. Singh and A. Gagliardi, *Sol. Energy*, 2019, **187**, 39–46.

6 A. Gagliardi and A. Abate, *ACS Energy Lett.*, , DOI:10.1021/acsenergylett.7b01101.

7 A. H. Fallahpour, A. Gagliardi, D. Gentilini, A. Zampetti, F. Santoni, M. Auf der Maur and A. Di Carlo, *J. Comput. Electron.*, , DOI:10.1007/s10825-014-0611-y.

8 A. H. Fallahpour, D. Gentilini, A. Gagliardi, M. A. Der Maur, P. Lugli and A. Di Carlo, *IEEE J. Photovoltaics*, , DOI:10.1109/JPHOTOV.2015.2486382.

9 A. Singh, E. Radicchi, S. Fantacci, F. De Angelis and A. Gagliardi, *J. Phys. Chem. C*, , DOI:10.1021/acs.jpcc.9b03658.

10 D. Gentilini, A. Gagliardi, A. A. Franco, F. Sauvage and A. di Carlo, *J. Electrochem. Soc.*, , DOI:10.1149/2.0061510jes.

11 R. Tagliaferro, D. Gentilini, S. Mastroianni, A. Zampetti, A. Gagliardi, T. M. Brown, A. Reale and A. Di Carlo, *RSC Adv.*, , DOI:10.1039/c3ra43380c.

12 D. Rossi, F. Santoni, M. Auf Der Maur and A. Di Carlo, *IEEE Trans. Electron Devices*, , DOI:10.1109/TED.2019.2912521.

13 A. Di Vito, A. Pecchia, A. Di Carlo and M. Auf Der Maur, *Phys. Rev. Appl.*, , DOI:10.1103/PhysRevApplied.12.014055.

14 T. Goudon, V. Miljanović and C. Schmeiser, *SIAM J. Appl. Math.*, , DOI:10.1137/060650751.

15 J. G. Simmons and G. W. Taylor, *Phys. Rev. B*, , DOI:10.1103/PhysRevB.4.502.

16 C. Wehrenfennig, G. E. Eperon, M. B. Johnston, H. J. Snaith and L. M. Herz, *Adv. Mater.*, , DOI:10.1002/adma.201305172.

17 Y. Hua, B. Xu, P. Liu, H. Chen, H. Tian, M. Cheng, L. Kloo and L. Sun, *Chem. Sci.*, , DOI:10.1039/c5sc03569d.

18 A. Wypych, I. Bobowska, M. Tracz, A. Opasinska, S. Kadlubowski, A. Krzywania-Kaliszewska, J. Grobelny and P. Wojciechowski, *J. Nanomater.*, , DOI:10.1155/2014/124814.

19 Z. Li, J. Chen, H. Li, Q. Zhang, Z. Chen, X. Zheng, G. Fang, H. Wang and Y. Hao, *RSC Adv.*, , DOI:10.1039/c7ra06643k.

20 A. J. MouÍ, H. J. Snaith, M. Kaiser, H. Klesper, D. M. Huang, M. Grätzel and K. Meerholz, *J. Appl. Phys.*, , DOI:10.1063/1.3204982.

21 T. Kirchartz, J. A. Márquez, M. Stolterfoht and T. Unold, , DOI:10.1002/aenm.201904134.

22 H. Fan, Z. Yang, X. Ren, M. Yin, F. Gao and S. F. Liu, *AIP Adv.*, , DOI:10.1063/1.4941040.

23 P. Wangyang, C. Gong, G. Rao, K. Hu, X. Wang and C. Yan, 2018, **1701302**, 1–30.

24 A. Singh and A. Gagliardi, *Proc. IEEE Conf. Nanotechnol.*, 2020, **2020**-**July**, 227–232.

25 D. Meggiolaro, E. Mosconi, A. H. Proppe, R. Quintero-bermudez, S. O. Kelley, E. H. Sargent and F. De Angelis, *ACS Energy Lett.*, 2019, **4**, 2181–2184.

26 C. C. Stoumpos, C. D. Malliakas and M. G. Kanatzidis, *Inorg. Chem.*, 2013, **52**, 9019–9038.

27 J. P. Perdew, K. Burke and M. Ernzerhof, *Phys. Rev. Lett.*, 1996, 3865–3868.

28 J. Heyd, G. E. Scuseria, M. Ernzerhof, J. Heyd, G. E. Scuseria and M. Ernzerhof, *J. Chem. Phys.*, , DOI:10.1063/1.1564060.

29 P. Umari, E. Mosconi and F. De Angelis, *Sci. Rep.*, 2014, **9**, 1–7.

30 E. Mosconi, P. Umari and F. De Angelis, *Phys. Chem. Chem. Phys.*, 2016, 27158–27164.

31 D. Meggiolaro and F. De Angelis, *ACS Energy Lett.*, 2018, **3**, 2206–2222.